



1 **Strong downdrafts preceding rapid tropopause ascent and their potential to**
2 **identify cross-tropopause stratospheric intrusions**

3 Feilong Chen¹, Gang Chen^{1*}, Chunhua Shi², Yufang Tian³, Shaodong Zhang¹,
4 Kaiming Huang¹

5 ¹School of Electronic Information, Wuhan University, Wuhan 430072, China.

6 ²Key Laboratory of Meteorological Disaster, Ministry of Education, Nanjing
7 University of Information Science & Technology, Nanjing 210044, China.

8 ³Key Laboratory of Middle Atmosphere and Global Environment Observation,
9 Institute of Atmospheric Physics, Chinese Academy of Sciences, Beijing 100029,
10 China

11 *Corresponding author: Gang Chen (g.chen@whu.edu.cn)

12

13 **Abstract:**

14 The capability of measuring 3-dimensional wind and tropopause structure with
15 relatively high time and vertical resolution makes VHF radar a potentially significant
16 tool for studying various processes of the atmosphere. Here the potential detection of
17 possible stratospheric intrusion events is discussed using the Beijing MST radar located
18 at Xianghe (39.75°N, 116.96°E). During the passage of a cut-off low in late November
19 2014, a deep V-shaped tropopause structure, and strong downdrafts (>0.8 m/s)
20 immediately preceding the rapid tropopause ascent (>0.2 km/h) were observed. Within
21 the height region of the downdrafts, the ‘normal’ radar-tropopause layer seems to be
22 destroyed (weakened) with the decreased echo intensity. Analysis results from global



23 reanalysis and the satellite data, as well as the trajectory model have shown the clear
24 evidence of the downward stratospheric intrusions (dry ozone-rich and depleted
25 methane air) associated with the strong downdrafts. According to the previous studies
26 and the present case observation, the strong downdrafts preceding rapid tropopause
27 ascent are considered as a significant signature of stratospheric intrusions. Twenty
28 typical cases of such strong downdrafts, occurring during various synoptic processes in
29 different seasons, have been presented and 16 of them are exactly associated with some
30 form of stratospheric intrusions. Four years (2012-2015) of such downdrafts are further
31 discussed. The observations reveal that the strong downdrafts preceding the rapid
32 tropopause ascent can be a valuable diagnostic for monitoring intrusion events, which
33 will gain a better understanding of stratospheric intrusions in VHF radar observations.

34

35 **Keywords:** Stratospheric intrusions; strong downdrafts; rapid tropopause ascent; MST
36 radar; VHF radar; cut-off low

37



38 1. Introduction

39 The tropopause is a stable transition zone separating the vertically stable stratified
40 stratosphere from the active free troposphere. The stratospheric and tropospheric air are
41 remarkably different in their chemical and dynamical characteristics. The stratosphere
42 is dominantly high in ozone and potential vorticity (PV) content and low in water vapor
43 (WV) and methane (CH₄) concentration, while the troposphere is just on the contrary
44 (Holton et al., 1995). Consequently, the natural stable tropopause layer, characterized
45 by strong gradients of trace constituents and wind speeds, plays an important role in
46 stratosphere-troposphere exchange (STE) processes. In other words, the layer is a
47 significant barrier for the atmospheric transport between stratosphere and troposphere
48 (Mahlman, 1997). From a long-term point of view, the long-term seasonal variation of
49 the tropopause height determines the seasonal variation of the flux of stratospheric air
50 into the free troposphere (Appenzeller et al., 1996). Under the global climate warming
51 (e.g. the continuing rise in CO₂), the tropopause variation is also a significant factor
52 that must be considered when comes to the recovery of the stratospheric ozone
53 (Butchart et al., 2010; Chipperfield et al., 2017). On the other hand, the short-term
54 tropopause variability is sensitive to various meso- and small-scale atmospheric
55 processes, during which the folding/intrusion events commonly occur. This
56 characteristic of the tropopause change are sometimes directly used to detect the
57 tropopause folds (e.g. Rao et al., 2008; Alexander et al., 2012, and references therein),
58 but are less, if any, directly used to identify stratospheric intrusions. More detailed
59 analysis of the variability of high-resolution tropopause height and of course some other



60 parameters (e.g. 3-dimensional wind), and how the stratospheric air transport across the
61 tropopause into the troposphere will help us to yield better understanding of the
62 downward stratospheric intrusions (e.g. Sprenger et al., 2003; Leclair de Bellevue et al.,
63 2007; Das et al., 2016).

64 Photochemical production within the troposphere, although, is the main source of
65 tropospheric ozone, the influence of the downward stratospheric intrusions on the
66 tropospheric ozone content cannot be ignored (Oltmans and Levy II, 1992; Monks,
67 2000; Stevenson et al., 2006). Stratospheric intrusions bring dry ozone-rich air down
68 into the free troposphere (e.g. Stohl et al., 2000; Sørensen and Nielsen, 2001) and
69 sometimes even deep to the surface (e.g. Gerasopoulos et al., 2006; Ding and Wang,
70 2006; Lefohn et al., 2011). By now, it is well established that these intrusions of
71 stratospheric origin will significantly influence other trace gases (such as hydroxyl
72 (OH)) in the troposphere (Holton et al., 1995). These influences then will further
73 contribute to the change of radiative balance (Ramaswamy et al., 1992) and play an
74 important role in the radiative forcing of global climate change (Holton et al., 1995). It
75 is true that stratospheric intrusion events occur all over the world and in any season.
76 However, they are highly episodic in both vertical and isentropic (horizontal) directions
77 (Chen, 1995). Various dynamical and physical processes have been proposed to be
78 responsible for extra-tropical intrusion events. These mainly include tropopause folds,
79 stratospheric streamers and break-up, cut-off lows (COLs), wave breaking, and
80 mesoscale convective activities and thunderstorms (Stohl et al., 2003).

81 The certain dynamical and chemical characteristics of stratospheric air allow the



82 tracers, such as dry ozone-rich and high PV, to be proper indicators for the intrusions
83 penetrating down into the troposphere. Various methods are available to detect intrusion
84 events based on these tracers. Among them, balloon-borne ozonesonde sounding are
85 without doubt one of the most appropriate tools, but is limited by coverage (He et al.,
86 2011) and not possible to obtain continuous profiles with fine temporal resolution. In
87 contrast, the satellite-borne remote sensing instruments, such as Atmospheric Infrared
88 Sounder (AIRS), can provide nearly global coverage of various trace gases but have
89 limitations in vertical and temporal resolution. Another method for studying transport
90 processes is trajectory model, from which the backward trajectories can provide
91 valuable information on the possible sources of the trace gases (e.g. Elbern et al., 1997).

92 By far, large-scale STE has been widely studied and is fairly well understood, but
93 the details of small scale intrusions are still remain uncertain (Holton et al., 1995).
94 Kumar and Uma (2009) reported that the dearth of direct vertical wind measurements
95 in the vicinity of the tropopause may be responsible for the lack of detailed fine
96 observations of smaller scale intrusions.

97 Very-High-Frequency (VHF) radars, comparing the tools mentioned above, are
98 capable to provide 3-dimensional wind and tropopause height continuously with both
99 high temporal and spatial resolution and can operate unmanned continuously for 24
100 hours per day under any weather conditions. During the past two decades, VHF radar
101 measurements were commonly used to assist to study the stratospheric intrusions.
102 However, it still remains uncertain in many aspects when using only the VHF radar to
103 identify intrusion events. Complicated and changeable atmospheric processes make it



104 difficult to identify the intrusion events by only radar data. The research by Hocking et
105 al., (2007) have achieved a development in this issue. They found that the rapid ascent
106 in radar-derived tropopause altitude (>0.2 km/h) can be a valuable diagnostic for
107 possible stratospheric intrusions. However, it does not always work (e.g. He et al., 2011)
108 and remains uncertain when purely using the information of radar-determined
109 tropopause.

110 The central objective of the present study is to discuss the signature of downward
111 cross-tropopause intrusions using both the measurements of tropopause height and
112 vertical wind by the Beijing MST radar. This study is carried out mainly via a detailed
113 case observation during the passage of a COL and other general cases associated with
114 various atmospheric processes. Our discussion mainly focused on the potential of the
115 MST radar data to identify possible intrusion events, which is the main point of this
116 paper. In section 2 the datasets used in this paper are described, section 3 presents
117 detailed results and discussion, and section 4 gives the conclusions.

118



119 2. Dataset

120 2.1. MST radar data and tropopause detection

121 The Beijing MST radar located at Xianghe, China (39.75° N, 116.96° E, 22 m
122 above sea level) is a VHF radar operated at 50 MHz and installed in 2010 based on the
123 first phase of Chinese Meridian Space Weather Monitoring Project (Chinese Meridian
124 Project for short) (Wang, 2010). The radar antenna array consists of 24×24 three-
125 element Yagi to produce an average power aperture product of $3.2 \times 10^8 \text{ Wm}^2$ and
126 maximum directive gain of 34.8 dB. It operates radiation pattern with 172 kW peak
127 power and 3.2° half-power beam width. More detailed information of the radar system
128 can be found in Chen et al. (2016). Routine low mode data were used for present study
129 with 0.5 h time resolution and 1 μs coded pulse, which provides 150 m vertical
130 resolution. Details of the low mode setup used in this study are given in Table 1.

131 It has long been known that VHF radar reflectivity is proportional to the mean
132 generalized refractive index gradient M , which is a function of humidity variation and
133 static stability and given by (Ottersten, 1969) as follows

$$134 \quad M = -77.6 \times 10^{-6} (p/T) (d \ln \theta / dz) \\ 135 \quad \cdot \{ 1 + 15500 q / T [1 - (d \ln q / dz) / (2 d \ln \theta / dz)] \} \quad (1)$$

136 where p is the atmospheric pressure (hPa) T is the temperature (K), θ is the potential
137 temperature (K) and q is the specific humidity (gg^{-1}). According to the second and third
138 terms of the equation (1): large humidity variation contributes to the echo from the
139 lower and middle troposphere. From the first term: the radar backscatter power is
140 proportional to the static stability, which in fact is directly proportional to the potential



141 temperature gradient. The tropopause, near which a strong potential temperature
142 gradient exists, will lead to strong radar echoes in vertical incidence, as well as large
143 radar aspect sensitivity (as shown in Figure 1). Radiosonde data used in this paper were
144 received from the GTS1 type digital radiosonde launched from Beijing Meteorological
145 Observatory (39.93 °N, 116.28 °E, station number 54511), which is less than 45 km to
146 the MST radar site. The black line in Fig.1 denotes the lapse-rate tropopause (LRT)
147 defined using the temperature lapse rate (World Meteorological Organization (WMO),
148 1986). Applying the characteristic (partial specular reflection) mentioned above, the
149 tropopause can be detected and its height determined by VHF radars (Gage and Green,
150 1979). It has received widespread application around the world, either in middle
151 latitudes (e.g. Hocking et al., 2007), polar regions (e.g. Alexander et al., 2012), and
152 tropical regions (e.g. Yamamoto et al., 2003; Das et al., 2008). Here, the radar-
153 determined tropopause (RT) height is defined as the lower edge (the height above 500
154 hPa with largest power gradient) of the secondary maximum backscattered echo power
155 (shown in Figure 1a as the orange circle). This definition of RT is similar to that in the
156 studies of Alexander et al., 2012 and Ravindrababu et al., 2014.

157 In the present study, the MST radar mainly provides continuous measurements of
158 backscattered echo power, 3-D wind, and RT height with time resolution of 0.5 hour. In
159 addition, the radar aspect sensitivity that expressed as the ratio between vertical (p_v)
160 and oblique (p_o) beam echo power is mainly caused by the horizontally stratified
161 anisotropic stable air and thus will be used as potential signature of stratospheric
162 intrusions in the troposphere (e.g. Kim et al., 2001). The backscattered echo power



163 given here is expressed as relative power in decibels (dB). In order to reduce the random
164 noise, the profile of p_v is smoothed by a 3-point running mean in altitude. Note that
165 the data that are heavily contaminated will be eliminated from our datasets. The data of
166 Dec. 2015 and Sep. 2015 are excluded.

167 2.2. AIRS satellite data

168 The AIRS instrument on NASA Aqua/EOS polar orbit satellite is a 2378 channel
169 nadir cross-track scanning infrared spectrometer. It can provide profiles of a number of
170 trace gases, including ozone and CH₄ (Susskind et al., 2003). The footprint of these
171 retrieval data is of 45 km by 45 km and their most sensitive region is in an altitude range
172 of 300-600 hPa. Many studies have shown that these AIRS retrieval constituents are
173 useful indicators for detecting stratospheric intrusions. He et al. [2011] suggested that
174 AIRS can observe the enhanced tropospheric ozone that is of stratospheric origin.
175 Xiong et al. [2013] reported that AIRS is capable of observing abnormal depletion in
176 CH₄ in the troposphere during intrusions. AIRS offers good latitude-longitude coverage.
177 Here we use version 6 of the AIRS Level-3 ozone and methane retrieval products.

178 2.3. Meteorological reanalysis

179 European Centre for Medium-Range Weather Forecasts (ECMWF) reanalysis
180 ERA-interim data are also used. After Nov. 2000 the data are based on the T511L60
181 version available with a 6-h temporal resolution and $3^\circ \times 3^\circ - 0.125^\circ \times 0.125^\circ$
182 latitude-longitude grid. The dataset from 15 isentropic and 37 pressure levels with
183 $0.5^\circ \times 0.5^\circ$ grid are applied for present study.

184 2.4. HYSPLIT model



185 Backward (forward) trajectories in given starting locations are capable to
186 reproduce the sources (destinations) of the air parcel that will allow us to examine the
187 intrusions of stratospheric origin in the troposphere (e.g. Elbern et al., 1997). The
188 Hybrid Single Particle Lagrangian Integrated Trajectory model (HYSPLIT) developed
189 by the National Oceanic and Atmospheric Administration (NOAA)'s Air Resource
190 Laboratory (ARL) (Rolph, 2003; Stein et al., 2016) is applied to calculate the backward
191 and forward trajectories. The calculation method of the model is a hybrid between the
192 Lagrangian approach and the Eulerian methodology. In this paper, Global Data
193 Assimilation System (GDAS) datasets are adopted for driving the HYSPLIT.
194



195 **3. Results and discussion**

196 3.1. Meteorological synoptic situation

197 On the morning of 29 November 2014, a 500-hPa trough developed on the western
198 side of Lake Baikal (Western Siberia). The trough moved southeastward and extended
199 equatorward and its bottom separated from the westerlies in the afternoon of 30
200 November 2014 (Fig. 2b), forming a COL near the radar site. The black stars in Figure
201 1 and other figures indicate the location of the radar site. On the following days, the
202 COL system moved northeastward gradually (Fig. 2b) and finally stayed over eastern
203 Russia near Sakhalin Island until it reconnected and merged to the westerly flow. 315
204 K isentropic PV patterns have shown the coarse resolution features of intrusions from
205 the polar reservoir across the tropopause into the midlatitude troposphere. The PV
206 streamer curved and rolled up cyclonically along the western flank of the COL (Fig.2b).

207 Fig. 3 shows the time series of hourly surface meteorological parameters over the
208 Beijing station. The data are obtained from the Chinese National Meteorology
209 Information Center and is less than 50 km from the MST radar site. As the dry-cold air
210 invasion accompanied with the COL travelled deeply into the planetary boundary layer,
211 it brought severe weather to the surface, including a rapid decrease in temperature and
212 humidity, and rapid increase in surface wind and sea level pressure. The humidity
213 decreased from ~85 to 12 percent within less than 8 hours. It is well established that the
214 polar-type COLs have strong potential to trigger deep convection (Price and Vaughan,
215 1993). To examine the potential convection, maps of high quality Climate Data Record
216 (CDR) of daily Outgoing Longwave Radiation (OLR) are displayed in Fig. 4. During



217 the development of the COL, a local region with abnormal low OLR value was clearly
218 observed near the radar site on 29 Nov. (Fig. 4b). The Satellite-observed cloud top
219 temperature also showed the low values corresponding to the low OLR (figure not
220 shown), indicating a convection may be generated near radar side on 29 Nov.. Please
221 note that we didn't observe such low value either in OLR (Fig.4c, d) or in cloud top
222 temperature near the radar side on 30 Nov. and 1 Dec.. The time for all the observations
223 in this paper is showed in Universal Time (UTC) which is eight hours behind Beijing
224 standard time ($LT=UT+8$).

225 **3.2. MST radar observations**

226 Radar echo power, horizontal wind vector, vertical wind, and radar aspect
227 sensitivity are plotted in Figure 5 as function of height and time during the passage of
228 the COL. Time variation of RT (black line) and LRT (black crosses) heights are also
229 displayed. The RT height first experienced a rapid descent, and then increased rapidly,
230 forming a deep V-shaped structure of ~4 km depth. The vertical velocity of the RT
231 height variation (both the rapid descent and ascent branches) reaches up to 0.28 km/h.
232 The rapid RT variation in altitude is in fact the response of the tropopause fold below
233 the jet stream, which will be well represented in Fig. 9a. Rapid variation in RT height
234 remained a region with low echo power (marked by R on Fig. 5a) and low aspect
235 sensitivity (marked by R' on Fig. 5d) where they should be normally high value within
236 the 'normal' tropopause layer. Unlike the RT height, the radiosonde LRT altitudes are
237 nearly constant during the COL passage. In normal conditions, RT agrees well with the
238 LRT altitude, such as indicated by Fig. 6a. However, large differences, of order of 2.5



239 km (as shown in Fig.6b at 12 UT 30 Nov.), are observed between LRT and RT in
240 altitude during the passage of the COL as expected. It is the difference in definition that
241 contribute most to the large differences, especially under the tropopause fold conditions.
242 It is worth noting that, in Fig.6b, although there is no clear reversion in the radiosonde
243 temperature profile within the height of RT, the RT height exactly corresponds well to
244 the reversion of zonal and meridional wind and potential temperature gradient. Such
245 differences between RT and LRT heights can commonly be observed, especially during
246 extreme synoptic situations such as cyclone (e.g. Alexander et al., 2012).

247 The most important observation in this detailed case experiment is the strong
248 downdrafts (hereinafter inferred to as main downdrafts) observed immediately
249 preceding the rapid RT ascent (Fig.5c). The radar echo power sharply weakened (dotted
250 rectangle in Fig.5a) and the wind direction changed rapidly (Fig.5b, change from
251 dominant southerly wind to dominant northerly jet) within the height region of the main
252 downdrafts. As mentioned previously, abnormal low value in OLR and cloud top
253 temperature indicates the possible occurrence of convective activity on 29 Nov., but
254 nothing special appeared on 30 Nov. near radar site. Consequently, we preliminarily
255 consider that the main downdrafts occurred near 07 UT 30 November might not be
256 produced directly by convective activity. Here, the accurate origin of the main
257 downdrafts will not be discussed in detail, and it is also beyond the scope of present
258 study.

259 The research by Hocking et al. (2007) has suggested that the rapid RT ascent (>0.2
260 km h^{-1}) can be a valuable indicator for the occurrence of stratospheric intrusions. Here



261 in this paper, the main downdrafts preceding the rapid RT ascent observed by the
262 Beijing MST radar are thus suspected to be an important feature or response of some
263 form of vertical stratospheric intrusions. It is indeed reasonable. Firstly, as the
264 tropopause descends (folded downward), it will displace stratospheric air into the
265 troposphere (e.g. Hoskins et al., 1985). Secondly, the main downdrafts will act as an
266 effective way to weaken the tropopause by means of continuously impinges on the
267 tropopause, through which the stratospheric air is permitted to penetrate down into the
268 free troposphere (e.g. Hirschberg and Fritsch, 1993; Kumar, 2006). In addition, after
269 the main downdrafts, the observed region near the upper troposphere with strong
270 backscatter echoes (marked by Q) and especially with abnormal high aspect sensitivity
271 (marked by Q') may also be a weak signature of the possible intrusions. In normal
272 conditions in the upper-troposphere, they are usually low in value (such as the region
273 marked by P and P'). As we mentioned before, the large value in radar aspect sensitivity
274 is mainly caused by reflection from stable atmospheric layer, such as the tropopause or
275 lower-stratosphere. When stable stratospheric air intrudes into the troposphere and
276 without mixing with the surrounding air mass, the intrusions in the free troposphere
277 will be reflected as abnormal large aspect sensitivity. Further direct evidence of the
278 relevant intrusions in dynamical and chemical aspects will be demonstrated in next
279 section, using satellite AIRS and global reanalysis data.

280 Someone may be interested to notice the laminar periodic downdrafts and updrafts
281 near RT height for ~16 UT 30 Nov.-2 UT 1 Dec.. It is likely to be associated with
282 mountain wave activity induced by northerly jet. As shown in Supplementary figure S1,



283 there is relatively higher topography (~1000 m mountains) located in the north of the
284 radar site. To examine this aspect in detail, Fig. 7b shows the wavelet spectra of the
285 vertical wind in the lower stratosphere (at ~12.4 km, Fig. 7a). Results reveal the wave
286 activity with a period of ~3.5 hours and amplitude of ~1.1 m s⁻¹.

287 3.3. Associated stratospheric intrusions

288 Due to the sensitivity of the AIRS retrieved ozone and CH₄ is between 300-600
289 hPa. Fig. 8 shows the 500 hPa distribution of AIRS observed ozone and CH₄, along
290 with the AIRS tropopause contour (defined based on the temperature lapse-rate). The
291 ozone distribution maps (left panels of Fig. 8) clearly show a large area with enhanced
292 tropospheric ozone (>80 ppbv) near the radar site during the passage of the COL.
293 Moreover, severe CH₄ depletion (<1840 ppbv) was also observed (right panels in Fig.8).
294 These features of the ozone enhancement, CH₄ depletion, and the corresponding low
295 tropopause altitude clearly support the evidence of vertical downward cross-tropopause
296 stratospheric intrusions on 30 Nov..

297 The vertical cross-section of ECMWF PV and specific humidity at 1800 UT 30
298 November 2014 and the daily AIRS ozone on 30 November 2014, along with a constant
299 latitude 40° N, is shown in Fig. 9. The corresponding vertical structure of the
300 stratospheric intrusions (dry ozone-rich and high PV along with low tropopause) over
301 regions near radar side is clearly seen. The specific humidity tracer displays less distinct
302 structure as compared with the other two tracers (similar as that shown by Vèrèmes et
303 al., 2016). The cross-section of PV in Fig. 9a have demonstrated relatively finer-scale
304 structure of the stratospheric PV intrusions (below the jet stream), which penetrated



305 down deeply into ~650 hPa (~3.6 km).

306

307 3.4. Trajectory model analysis

308 Figure 10 shows 30h backward trajectories ending at the radar site at 18 UT 29
309 November (left panel) and at 18 UT 30 November (right panel). As expected, the air
310 masses parcel transported eastward horizontally before the occurrence of main
311 downdrafts (fig.10a). Whereas after the downdrafts, the trajectories clearly show that
312 the tropospheric air masses over the radar site are of stratospheric origin from the
313 western side of Lake Baikal. Trajectory results further support the evidence of
314 stratospheric intrusions that closely related with the main downdrafts.

315 On the other hand, 30-h forward trajectories starting at 00 UT 30 November (left
316 panel) and 00 UT 1 December (right panel) are shown in Fig. 11. It is interesting to note
317 that, from Fig.11a before the passage of COL, the air parcels at 4 km transport rapidly
318 upward (by more than 4 km within ~23 h) and northeastward to the upper-troposphere
319 of East Siberian. This upward and poleward transportation is associated with a warm
320 conveyor belt (dominate southerly flows) that is located ahead of the COL. It
321 contributes to transporting the tropospheric moist and polluted air (such as aerosol) into
322 the upper-troposphere and even the lower stratosphere (e.g. Stohl et al., 2003; Sandhya
323 et al., 2015). After the downdrafts, forward trajectories in fig.11b demonstrate that the
324 dry intrusion air parcels continue to be transported downward and southeastward to the
325 boundary layer or even the surface.

326 3.5. Strong downdrafts preceding rapid tropopause ascent and discussion



327 Figure 12a shows another 20 typical cases with strong downdrafts preceding rapid
328 RT ascent for the period Mar. 2012 and Jan. 2015 (shown placed end-to-end), and the
329 LRT height (plotted in crosses) and the vertical velocity of the RT (plotted in orange
330 line) is also plotted. These cases (marked by black rectangular boxes) are identified
331 based on the following criteria: 1) the amplitude of the RT ascent should exceed 0.6 km
332 (four range gates), 2) vertical velocities of the RT ascent excess 0.1 km/h, 3) the
333 downdrafts occurred preceding the RT ascent should reach at least 0.5 m/s, and the
334 height region of the downdrafts should pass through the RT layer. The criteria are put
335 forward mainly to avoid the influence of the RT spikes. Figure 12b shows the selected
336 9 cases of possible intrusions by means of the backward trajectories. Results show clear
337 evidence of possible stratospheric intrusions corresponding to the associated strong
338 downdrafts. Their sources are mainly from West Siberia (western side of Lake Baikal),
339 except for the case Tr5. Moreover, according to AIRS daily 500 hPa ozone distribution,
340 almost every case in Figure 12a (except for the cases labeled as A, B, C and D in Figure
341 12a) were associated with some form of significant ozone enhancement, indicating
342 intrusions of stratospheric origin (as shown in Supplementary figure S2). It is important
343 to note that the RT excursion velocity of all the cases is not all above 0.2 km/h and some
344 are lower than this value (e.g. case on 2 May. 2014). However, some form of
345 stratospheric intrusions were exactly observed in such case from both the trajectory and
346 satellite results. Therefore, the threshold of vertical velocity of the RT is set at 0.1 km/h,
347 rather than 0.2 km/h (Hocking et al., 2007). Large differences between RT and LRT are
348 also interesting to be noted on some occasions when the RT changes rapidly (such as



349 the occasion near 14 Mar. 2012).

350 According to the meteorological chart, the synoptic situation of those cases
351 identified in Fig.12a are introduced. The cases occurred on 6 Mar. 2012, 13 Jun. 2012,
352 and 31 Dec. 2012 seem to have a close relationship with the COL development; cases
353 on 13 Mar. 2012, 5 Apr. 2012, 6 Apr. 2012, 4 Jan. 2014, and 2 May 2014, seem
354 associated with low or high pressure systems. The remaining cases seem not associated
355 with any significant synoptic development. However, in terms of the distribution of
356 isentropic PV (generally at 315K in winter and 330K in summer), we found that the
357 remaining cases occurred on 3 Aug. 2013, 3 Jan. 2014, and 3 Jan. 2015 appear to be
358 associated with some form of stratospheric streamers and their break-up within the
359 previous 48h. Some cases (e.g. A and B) that appear close on the same day were
360 probably caused by the same system and not possible to examine the associated possible
361 intrusions separately using either the reanalysis or satellite data.

362 In the light of present understanding, the strong downdrafts preceding the rapid
363 RT ascent can serve as an important predictor for intrusion events, during any synoptic
364 processes in any season. This characteristic will be of great use and play an important
365 role in routine identification or prediction of stratospheric intrusions. Considering the
366 duration of such downdrafts, a higher time resolution of radar observations will be more
367 helpful. Present study have shown the duration of the majority downdrafts is generally
368 within 1.5-3 hours. We consider, therefore, that the radar resolution should be best
369 within 1h.

370 Although Hocking et al. (2007) have reported that the rapid tropopause ascent



371 (>0.2 km/h) alone can be a useful diagnostic for potential intrusion events. However,
372 using only the information of RT heights might lead to non-negligible errors, as
373 mentioned above in introduction and according to the observations in Fig. 12.
374 Especially on occasions when the RT ascent is between 0.1-0.2 km/h but the
375 corresponding true intrusions were observed, all such intrusion events will be neglected
376 (maybe ~2 per month, refer to Fig. 13a). Whereas on some occasions when the RT
377 ascent excess 0.2 km/h, but without observing true intrusion events (e.g. He et al., 2011),
378 these events will be misdiagnosed (maybe ~13 per month, refer to Fig. 13b). In this
379 sense, using the unique MST radar observations of both the RT height variability and
380 the vertical wind as complementary signature for identifying possible intrusion events
381 is very meaningful.

382 Figure 13 shows four years (2012-2015) of the events with rapid RT ascent (gray
383 bands), and the events with strong downdrafts just preceding the rapid RT ascent (black
384 bands). The identification criteria of such strong downdrafts are similar to that
385 mentioned above and the events are classified according to different value of vertical
386 velocity of the ascent. Among all the events with ascent velocity between 0.1-0.2 km/
387 h, about one-quarter (approximate 2 per month, Fig. 13a) were observed with strong
388 downdrafts preceding them. Whereas, as for the events with the ascent velocity >0.2
389 km/h, the proportion is about a half (approximate 10 per month, Fig. 13b). Here,
390 according to the results above, the occurrence of the strong downdrafts just preceding
391 the rapid RT ascent (black bands in Fig. 13) to a large degree represents the occurrence
392 of possible intrusions. In this way, Fig. 13 indicates that the occurrence of possible



393 intrusions exhibit distinct seasonal variations, with a maximum in winter and spring
394 minimum in summer. This is because the meso- and small-scale atmospheric processes,
395 such as cold air outbreaks, thunderstorms, and convective activities, are more active in
396 winter and spring. They are important sources for downward stratospheric intrusions.
397



398 **4. Conclusions**

399 Detailed case analysis of the cross-tropopause stratospheric intrusions was carried
400 out during a COL. Global reanalysis, satellite data, and HYSPLIT trajectories all
401 showed consistent evidences of dry ozone-rich, high PV, and depleted CH₄ air that have
402 penetrated downward into the free troposphere. The key signature of the stratospheric
403 intrusions in the Beijing MST radar observations is the strong downdrafts just preceding
404 rapid RT ascent. The radar echo power decreased rapidly within the region of strong
405 downdrafts, after which abnormal high aspect sensitivity was recorded in troposphere.
406 Such high aspect sensitivity is served as another potential clue for the intrusions of
407 stratospheric origin. By means of wavelet spectra analysis, the periodic perturbation
408 with period of ~3.5 h is found in vertical wind in the lower stratosphere. This
409 perturbation is probably related to the mountain wave activity induced by northerly jet.

410 Based on the criteria mentioned in section 3.5, other 20 typical cases of strong
411 downdrafts preceding the rapid RT ascent between Mar. 2012 and Jan. 2015 were
412 presented. These events occurred during different synoptic processes in different
413 seasons. What counts is, almost all the cases (16 of them) are associated with some
414 form of intrusions observed by combination of AIRS retrieved ozone and the HYSPLIT
415 trajectory model. Our results show that the radar derived tropopause height and vertical
416 winds are strong complementary indicators to be used to infer the occurrence of the
417 intrusions of stratospheric origin. This will be of great use and play an important role
418 for the routine identification or prediction of intrusion events. However, the actual
419 origin of the observed downdrafts preceding the rapid RT ascent is not addressed in this



420 paper. Further combination observational experiments need to be conducted, especially

421 combined using ozonesonde soundings, to quantitative analyze the effectiveness of

422 present identification criteria for possible intrusions.

423

424



425 **Acknowledgment**

426 The authors really appreciate Prof Shira Raveh-Rubin for reading and checking the
427 manuscript, using the criterion in Raveh-Rubin, 2017. This work is funded by National
428 Natural Science Foundation of China (NSFC grants No. 41722404 and 41474132). The
429 authors would like to thanks the technical and scientific staff of Chinese Meridian Space
430 Weather Monitoring Project (CMSWMP) for their support in conducting the
431 experiment. The authors sincerely acknowledge the ECMWF, NASA, and NOAA Air
432 Resources Laboratory (ARL) for providing global reanalysis, satellite trace gases, and
433 HYSPLIT transport model, respectively. The MST radar data for this paper are
434 available at Data Centre for Meridian Space Weather Monitoring Project
435 (<http://159.226.22.74/>). The radiosonde data is available from
436 <http://weather.uwyo.edu/upperair/sounding.html>.

437



438 **References**

- 439 Appenzeller, C., Holton, J. R., & Rosenlof, K. H.: Seasonal variation of mass transport
440 across the tropopause. *Journal of Geophysical Research Atmospheres*, 101(D10),
441 15071–15078, 1996.
- 442 Appenzeller, C., Davies, H. C., & Norton, W. A.: Fragmentation of stratospheric
443 intrusions. *Journal of Geophysical Research Atmospheres*. 101(D1), 1435-1456,
444 1996.
- 445 Alexander, S. P., Murphy, D. J., and Klekociuk, A. R.: High resolution VHF radar
446 measurements of tropopause structure and variability at Davis, Antarctica (69° S,
447 78° E). *Atmospheric Chemistry and Physics*, 13(12), 26173-26205, 2012.
- 448 Bonasoni, P., Evangelisti, F., Bonafe, U., Ravegnani, F., Calzolari, F., Stohl, A., Tositti
449 L., Tubertini O., & Colombo, T.: Stratospheric ozone intrusion episodes recorded
450 at Mt. Cimone during the VOTALP project: case studies. *Atmospheric*
451 *Environment*, 34(9), 1355-1365, 2000.
- 452 Butchart, N., Cionni, I., Eyring, V., Shepherd, T. G., Waugh, D. W., & Akiyoshi, H.,
453 et al.: Chemistry-climate model simulations of twenty-first century stratospheric
454 climate and circulation changes. *Journal of Climate*, 23(20), 5349-5374, 2010.
- 455 Chipperfield, M. P., Bekki, S., Dhomse, S., Harris, N., Hassler, B., & Hossaini, R., et
456 al.: Detecting recovery of the stratospheric ozone layer. *Nature*, 549(7671), 211-
457 218, 2017.
- 458 Chen, P.: Isentropic cross-tropopause mass exchange in the extratropics. *Journal of*
459 *Geophysical Research*, 16661-16673, 1995.



- 460 Chen, G., Cui, X., Chen, F., Zhao, Z., Wang, Y., Yao, Q., ... & Gong, W.: MST Radars
461 of Chinese Meridian Project: System Description and Atmospheric Wind
462 Measurement. *IEEE Transactions on Geoscience and Remote Sensing*, 54(8),
463 4513-4523, 2016.
- 464 Das, S. S., A. R. Jain, K. K. Kumar, and D. Narayana Rao: Diurnal variability of the
465 tropical tropopause: Significance of VHF radar measurements, *Radio Sci.*, 43,
466 RS6003, doi:10.1029/2008RS003824, 2008.
- 467 Das, S. S., Ratnam, M. V., Uma, K. N., Patra, A. K., Subrahmanyam, K. V., Girach, I.
468 A., Suneeth K. V. , Kumar K. K., & Ramkumar, G.: Stratospheric intrusion into
469 the troposphere during the tropical cyclone Nilam (2012). *Quarterly Journal of the*
470 *Royal Meteorological Society*, 142(698), 2168-2179, 2012.
- 471 Ding, A., and T. Wang: Influence of stratosphere-to-troposphere exchange on the
472 seasonal cycle of surface ozone at Mount Waliguan in western China, *Geophysical*
473 *Research Letters*, 33, L03803, doi.10.1029/ 2005GL024760, 2006.
- 474 Elbern, H., Kowol, J., Sládkovic, R., & Ebel, A.: Deep stratospheric intrusions: a
475 statistical assessment with model guided analyses. *Atmospheric Environment*,
476 31(19), 3207-3226, 2006.
- 477 Gage, K. S., & Green, J. L.: Tropopause detection by partial specular reflection with
478 Very-High-Frequency radar. *Science*, 203(4386), 1238-40, 1979.
- 479 Gerasopoulos, E., Zanis, P., Papastefanou, C., Zerefos, C.S., Ioannidou, A., Wernli, H.:
480 A complex case study of down to the surface intrusions of persistent stratospheric
481 air over the Eastern Mediterranean. *Atmospheric Environment*, 40(22), 4113-4125,



482 2006.

483 He, H., Tarasick, D. W., Hocking, W. K., Careysmith, T. K., Rochon, Y. J., Zhang, J., ...

484 & Bourqui, M. S.: Transport analysis of ozone enhancement in Southern Ontario

485 during BAQS-Met. *Atmospheric Chemistry and Physics*, 11(6), 2569-2583, 2011.

486 Hocking, W. K., Careysmith, T., Tarasick, D. W., Argall, P. S., Strong, K., Rochon, Y.

487 J., Zawadzki Irek & Taylor, P. A.: Detection of stratospheric ozone intrusions by

488 windprofiler radars. *Nature*, 450(7167), 281-284, 2007.

489 Holton, J. R., P. H. Haynes, M. E. McIntyre, A. R. Douglass, R. B. Rood, and L. Pfister:

490 Stratosphere-troposphere exchange, *Reviews of Geophysics*, 33(4), 403-439,

491 doi:10.1029/95RG02097, 1995.

492 Hoskins B.J., McIntyre M.E., Robertson A.W.: On the use and significance of

493 isentropic potential vorticity maps. *Q. J. R. Meteorol. Soc.* 111: 877-946. 1985.

494 Hirschberg, P. A., and J. M. Fritsch: A study of the development of extratropical

495 cyclones with an analytic model. Part I: The effects of stratospheric structure,

496 *Journal of the Atmospheric Sciences*, 50, 311 -327, doi:10.1175/1520-

497 0469(1993)050<0311:ASOTDO>2.0.CO;2, 1993.

498 Kim, K. E., Jung, E. S., Campistron, B., & Heo, B. H.: A physical examination of

499 tropopause height and stratospheric air intrusion: a case study. *Journal of the*

500 *Meteorological Society of Japan*, 79(5), 1093-1103, 2001.

501 Kumar, K. K., & Uma, K. N.: High temporal resolution VHF radar observations of

502 stratospheric air intrusions in to the upper troposphere during the passage of a

503 mesoscale convective system over gadanki (13.5° n, 79.2° e). *Atmospheric*



- 504 Chemistry & Physics, 24(8), 14-17, 2009.
- 505 Kumar, K. K.: VHF radar observations of convectively generated gravity waves: Some
506 new insights. *Geophysical Research Letters*, 33(1), doi:10.1029/2005GL024109,
507 2006.
- 508 Leclair de Bellevue J, Baray JL, Baldy S, Ancellet G, Diab R, Ravetta F.: Simulations
509 of stratospheric to tropospheric transport during the tropical cyclone Marlene
510 event. *Atmospheric Environment*. **41**: 6510–6526, doi:
511 10.1016/j.atmosenv.2007.04.040, 2007.
- 512 Lefohn, A. S., Wernli, H., Shadwick, D., Limbach, S., Oltmans, S. J., Shapiro, M.: The
513 importance of stratospheric–tropospheric transport in affecting surface ozone
514 concentrations in the western and northern tier of the United States. *Atmospheric
515 Environment*, 45(28), 4845-4857, 2011.
- 516 Mahlman, J. D.: Dynamics of transport processes in the upper troposphere. *Science*,
517 276(5315), 1079-1083, 1997.
- 518 Mihalikova, M., Kirkwood, S., Arnault, J., & Mikhaylova, D.: Observation of a
519 tropopause fold by MARA VHF wind-profiler radar and ozonesonde at Wasa,
520 Antarctica: comparison with ECMWF analysis and a WRF model simulation.
521 *Annales Geophysicae*, 30(9), 1411-1421, 2012.
- 522 Monks, P. S.: A review of the observations and origins of the spring ozone maximum,
523 *Atmospheric Environment*, 34, 3545–3561, 2000.
- 524 Nastrom, G. D., Green, J. L., Gage, K. S., & Peterson, M. R.: Tropopause folding and
525 the variability of the tropopause height as seen by the flatland VHF radar. *Journal*



- 526 of Applied Meteorology, 28(12), 1271-1281, 1989.
- 527 Oltmans, S. J., and H. Levy II.: Seasonal cycle of surface ozone over the western North
528 Atlantic, *Nature*, 358, 392–394, 1992.
- 529 Ottersten, H.: Mean vertical gradient of potential refractive index in turbulent mixing
530 and radar detection of CAT, *Radio Science*, 4, 1247–1249,
531 doi:10.1029/RS004i012p01247, 1969.
- 532 Price, J. D., & Vaughan, G.: The potential for stratosphere-troposphere exchange in cut-
533 off-low systems. *Quarterly Journal of the Royal Meteorological Society*, 119(510),
534 343-365, 1993.
- 535 Rao, T. N., and S. Kirkwood: Characteristics of tropopause folds over Arctic latitudes,
536 *Journal of Geophysical Research*, 110, D18102, doi:10.1029/2004JD005374,
537 2005.
- 538 Rao, T. N., Arvelius, J., & Kirkwood, S.: Climatology of tropopause folds over a
539 european arctic station (esrange). *Journal of Geophysical Research Atmospheres*,
540 113(D7), 762-770, 2008.
- 541 Ravindrababu, S., Venkat Ratnam, M., Sunilkumar, S. V., Parameswaran, K., and
542 Krishna Murthy, B. V.: Detection of tropopause altitude using Indian MST radar
543 data and comparison with simultaneous radiosonde observations. *Journal of*
544 *Atmospheric and Solar-Terrestrial Physics*, 121(6), 679-687, 2014.
- 545 Ramaswamy V, Schwarzkopf MD, Shine KP.: Radiative forcing of climate from
546 halocarbon-induced global stratospheric ozone loss. *Nature* **355**: 810–812, doi:
547 10.1038/355810a0, 1992.



- 548 Rolph, G.D.: Real-time Environmental Applications and Display sYstem (READY)
549 Website. NOAA Air Resources Laboratory, Silver Spring, MD. [http://](http://www.arl.noaa.gov/ready/hysplit4.html)
550 www.arl.noaa.gov/ready/hysplit4.html, 2003.
- 551 Sandhya, M., Sridharan, S., & Indira Devi, M.: Tropical upper tropospheric humidity
552 variations due to potential vorticity intrusions. *Annales Geophysicae*, 33(9), 1081-
553 1089, 2015.
- 554 Skerlak, B., Sprenger, M., Pfahl, S., Tyrlis, E., & Wernli, H.: Tropopause folds in ERA-
555 Interim: Global climatology and relation to extreme weather events. *Journal of*
556 *Geophysical Research*, 120(10), 4860-4877, 2015.
- 557 Stohl, A., Bonasoni, P., Cristofanelli, P., Collins, W., Feichter, J., & Frank, A., et al.:
558 Stratosphere-troposphere exchange: a review, and what we have learned from
559 staccato. *Journal of Geophysical Research Atmospheres*, 108(D12), 469-474,
560 2003.
- 561 Stohl, A., et al.: The influence of stratospheric intrusions on alpine ozone
562 concentrations, *Atmospheric Environment*, 34, 1323– 1354, 2000.
- 563 Stohl, A., Wernli, H., James, P., Bourqui, M., Forster, C., & Liniger, M. A., et al.: A
564 new perspective of stratosphere troposphere exchange. *Bulletin of the American*
565 *Meteorological Society*, 84(11), 2003.
- 566 Stein, A. F., Draxler, R. R., Rolph, G. D., Stunder, B. J. B., Cohen, M. D., & Ngan, F.:
567 Noaa's HYSPLIT atmospheric transport and dispersion modeling system. *Bulletin*
568 *of the American Meteorological Society*, 96(12), 150504130527006, 2016.
- 569 Stevenson, D. S., Dentener, F. J., Schultz, M. G., Ellingsen, K., Noije, T. P. C. V., &



- 570 Wild, O., et al.: Multimodel ensemble simulations of present-day and near-future
571 tropospheric ozone. *Journal of Geophysical Research Atmospheres*, 111(D8), 263-
572 269, 2006.
- 573 Sørensen, J. H., and Nielsen, N. W.: Intrusion of stratospheric ozone to the free
574 troposphere through tropopause folds -a case study. *Physics and Chemistry of the*
575 *Earth Part B Hydrology Oceans and Atmosphere*, 26(10), 801-806, 2001.
- 576 Su, L., Yuan, Z., Fung, J. C., & Lau, A. K.: A comparison of HYSPLIT backward
577 trajectories generated from two GDAS datasets. *Science of The Total Environment*,
578 527-537, 2015.
- 579 Susskind, J., C. D. Barnet, and J. M. Blaisdell.: Retrieval of atmospheric and surface
580 parameters from AIRS/AMSU/HSB data in the presence of clouds, *IEEE*
581 *Transactions on Geoscience and Remote Sensing*, 41(2), 390–409,
582 doi:10.1109/tgrs.2002.808236, 2003.
- 583 Vaughan, G., Gouget, H., O'Connor, F. M., & Wier, D.: Fine-scale layering on the edge
584 of a stratospheric intrusion. *Atmospheric Environment*, 35(12), 2215–2221, 2001.
- 585 Vérèmes, H., J.-P. Cammas, J.-L. Baray, P. Keckhut, C. Barthe, F. Posny, P. Tulet, D.
586 Dionisi, and S. Bielli: Multiple subtropical stratospheric intrusions over Reunion
587 Island: Observational, Lagrangian, and Eulerian numerical modeling approaches,
588 *Journal of Geophysical Research Atmospheres*, 121, 14,414–14,432, doi:10.1002/
589 2016JD025330, 2016.
- 590 Wang, C.: New Chains of Space Weather Monitoring Stations in China. *Space Weather-*
591 *the International Journal of Research and Applications*, 8(8), 2010.



- 592 World Meteorological Organization (WMO): Atmospheric ozone 1985, WMO Global
593 Ozone Res. and Monit. Proj. Rep. 20, Geneva, Switzerland, 1986.
- 594 Xiong, X., C. Barnet, E. Maddy, S. C. Wofsy, L. Chen, A. Karion, and C. Sweeney.:
595 Detection of methane depletion associated with stratospheric intrusion by
596 atmospheric infrared sounder (AIRS), Geophysical Research Letters, 40, 2455–
597 2459, doi:10.1002/grl.50476, 2013.
- 598 Yamamoto, M., Oyamatsu, M., Horinouchi, T., Hashiguchi, H., & Fukao, S.: High time
599 resolution determination of the tropical tropopause by the Equatorial Atmosphere
600 Radar. Geophysical Research Letters, 30(21), 2003.
- 601



602 **Table**

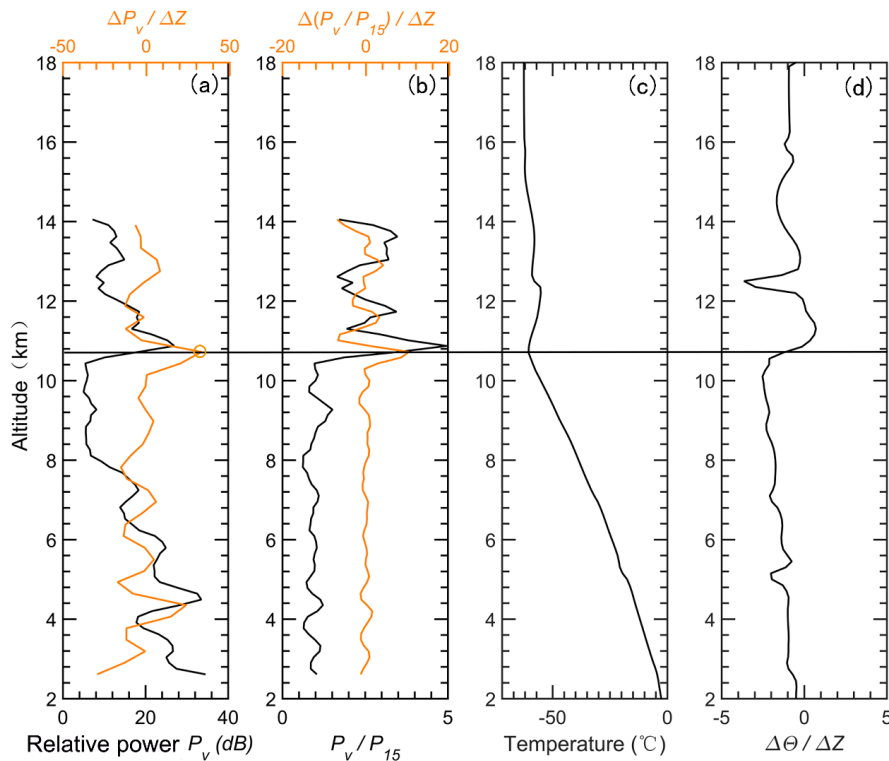
Radar parameter	Value
Transmitted frequency	50 MHz
Antenna array	24 × 24 3-element Yagi
Antenna gain	33 dB
Transmitter peak power	172.8 kW
Code	16-bit complementary
No. coherent integrations	128
No. FFT points	256
No. spectral average	10
Pulse repetition period	160 μs
Half power beam width	3.2°
Pulse length	1 μs
Range resolution	150 m
Temporal resolution	30 min
Off-zenith angle	15°

603 **Table 1.** Operating parameters in low-mode of the Beijing MST radar.

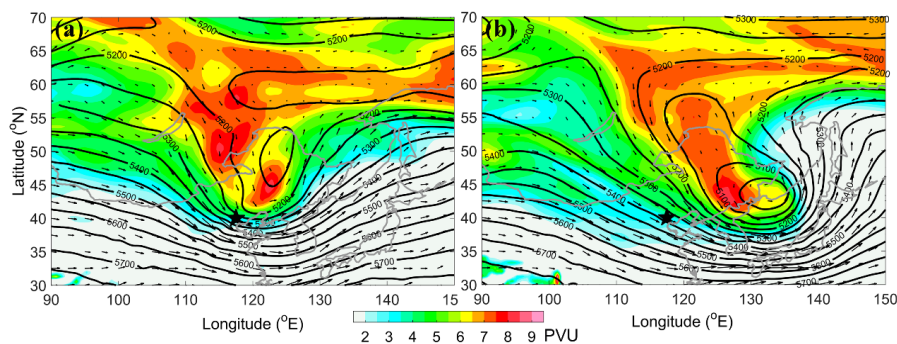
604



605 **Figures**

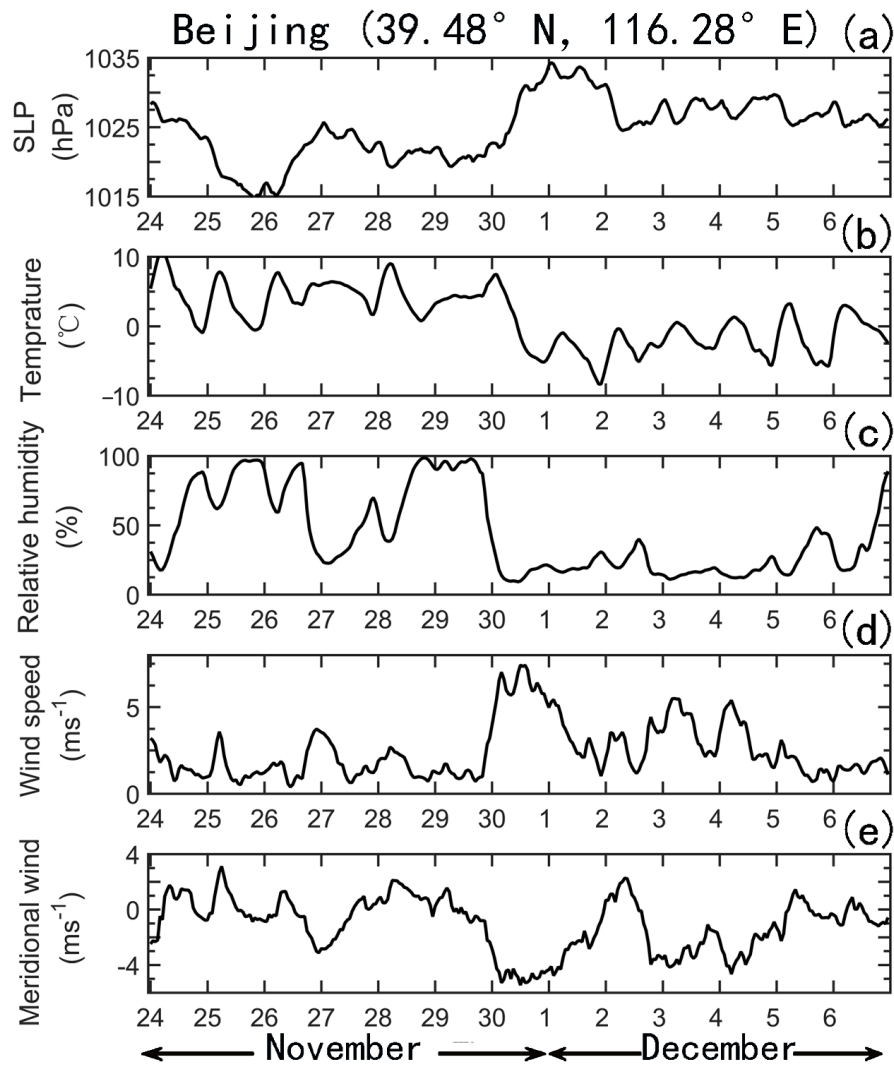


606
 607 **Figure 1.** Example of the vertical height profiles of (a) the relative radar echo power
 608 (black line, smoothed by a 3-point running mean) along with its gradient variation
 609 (orange line), (b) the aspect sensitivity (black line, expressed as the ratio between the
 610 vertical echo power and oblique echo power) along with its gradient variation (orange
 611 line), observed on 12 UT 29 November 2014. The vertical profiles of simultaneous
 612 radiosonde observed temperature and potential temperature gradient are shown in plots
 613 (c) and (d). The black horizontal line denotes the LRT height derived from the
 614 radiosonde temperature profile. The orange circle indicates the RT height derived from
 615 the profile of the radar backscattered echo power.



616

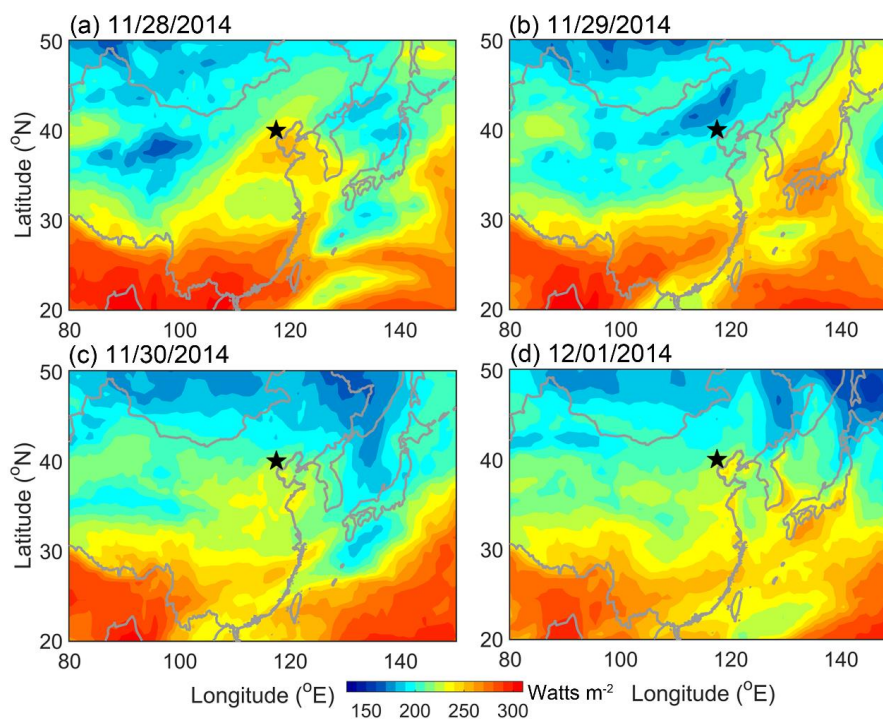
617 **Figure 2.** ECMWF derived isentropic PV map on 315 K surface (shaded above 2 pvu,
618 $1 \text{ PVU} = 10^{-6} \text{ m}^2 \text{ K kg}^{-1} \text{ s}^{-1}$) and geopotential height (contoured every 50 m in solid line)
619 along with the wind vector (arrow) at 500 hPa (~5.5 km a.s.l.) on (a) 18 UTC 30
620 November 2014, (b) 12 UTC 1 December 2014. The black star shows the location of
621 Xianghe.



622

623 **Figure 3.** Time series of surface (~ 1.2 m above the surface) hourly meteorological
624 measurements of (a) sea level pressure, (b) temperature, (c) relative humidity, (d)
625 horizontal wind, and (e) meridional wind during the period 24 Nov.-6 Dec. 2014,
626 observed over the Beijing station (39.4° N, 116.2° E, 31.3 m above sea level).

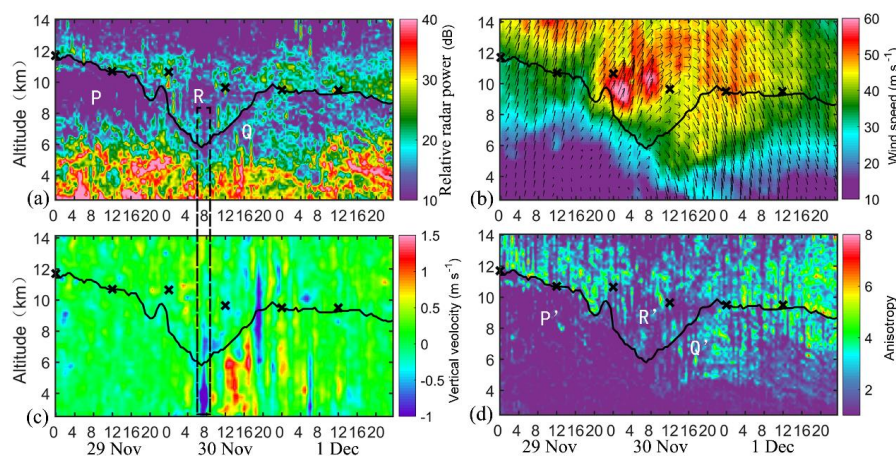
627



628

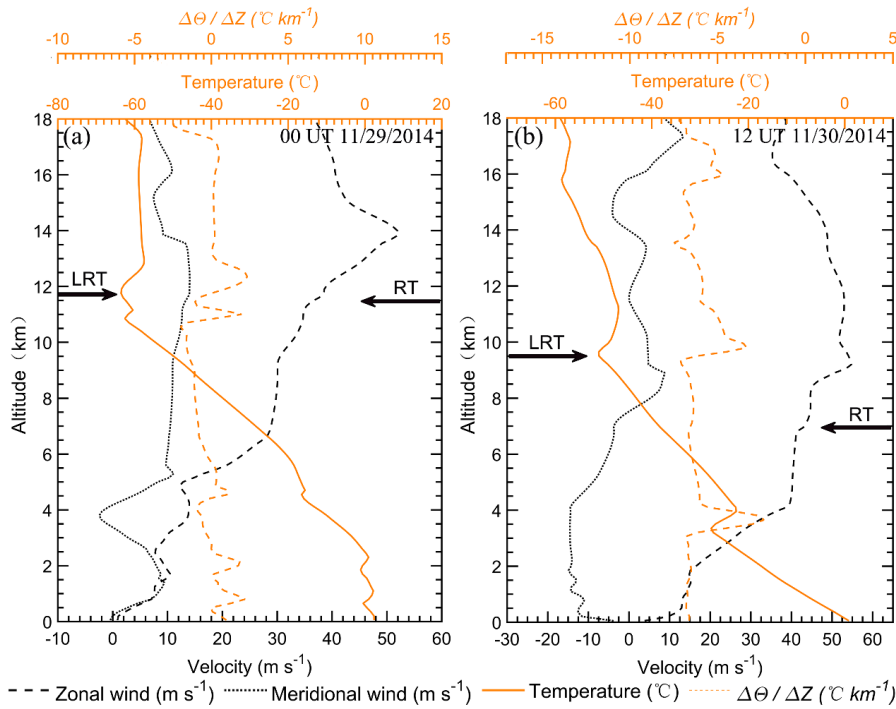
629 **Figure 4.** Contour maps of the high quality Climate Data Record (CDR) of the daily
630 Outgoing Longwave Radiation (OLR), derived from the NOAA high-resolution
631 infrared radiation sounder (HIRS) on (a) 28 Nov., (b) 29 Nov., (c) 30 Nov., and (d) 1
632 Dec. 2014. The black star shows the location of Xianghe.

633

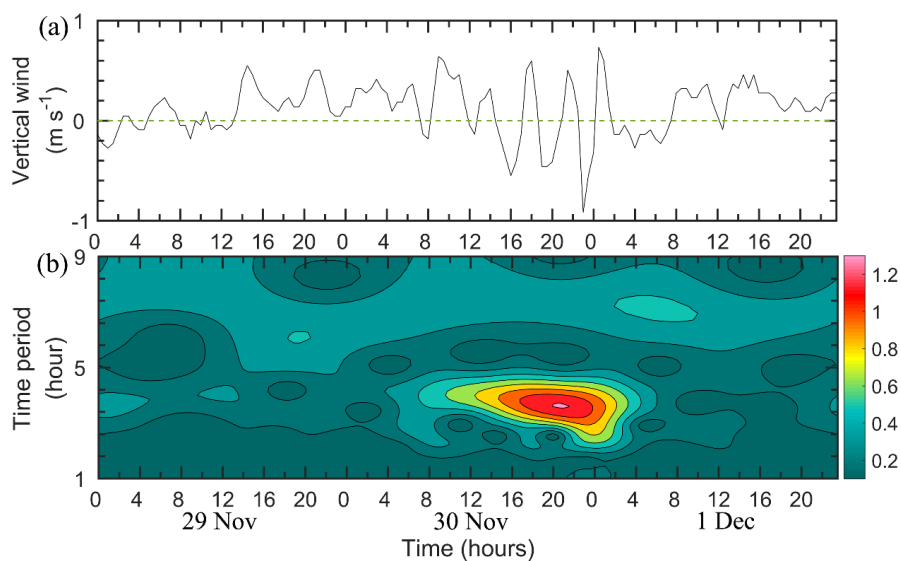


634

635 **Figure 5.** Altitude-time section of (a) the radar backscattered echo power in zenith
636 direction, (b) the horizontal wind speed along with wind vector, of which the up and
637 down arrows represent north and south respectively, and left-right is west-east, (c) the
638 vertical velocity, and (d) the aspect sensitivity, observed by the Beijing MST radar from
639 29 November to 1 December 2014. The black curve shows the radar-determined
640 tropopause, as defined in section 2.1. The dotted rectangle highlights the strong
641 downdrafts immediately preceding the rapid tropopause ascent. The positions of the
642 LRT tropopause heights, derived from the nearly simultaneous collocated GPS
643 radiosonde temperature profile, are marked by crosses.



644 --- Zonal wind (m s^{-1}) Meridional wind (m s^{-1}) — Temperature ($^{\circ}\text{C}$) - - - $\Delta\theta / \Delta Z$ ($^{\circ}\text{C km}^{-1}$)
 645 **Figure 6.** Vertical profiles of zonal wind, meridional wind, temperature, and potential
 646 temperature gradient derived from the GPS radiosonde measurements, at (a) 0000 UTC
 647 29 November 2014 and (b) 1200 UTC 30 November 2014. The bold arrows on the left
 648 and right side of each panel indicate the radiosonde derived LRT tropopause and radar-
 649 derived tropopause height, respectively.
 650

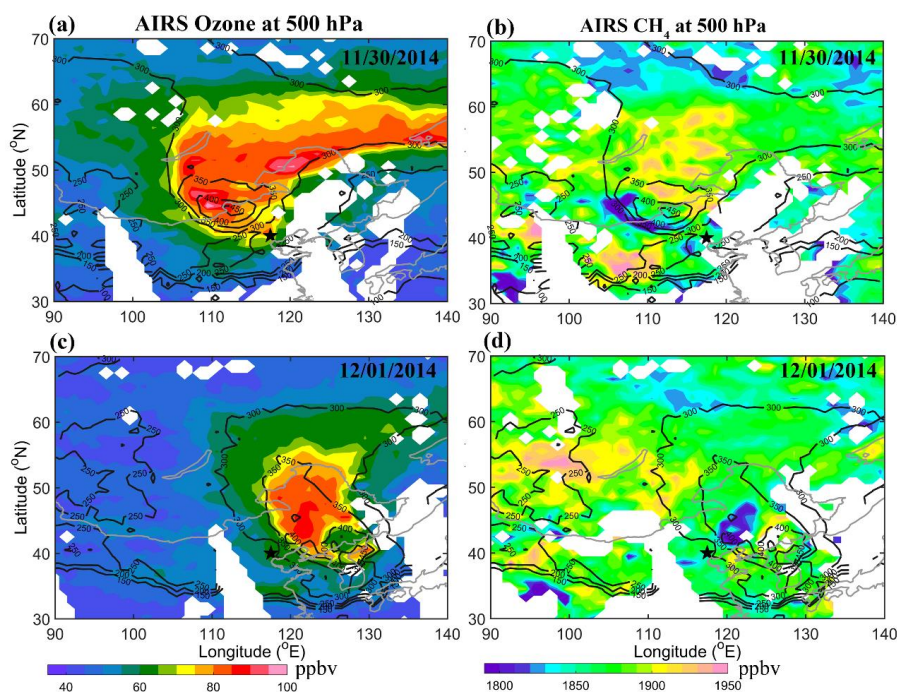


651

652 **Figure 7.** (a) Radar derived vertical velocity variations with time and (b) wavelet

653 spectra analysis of the vertical velocity at ~ 12.4 km in the lower stratosphere.

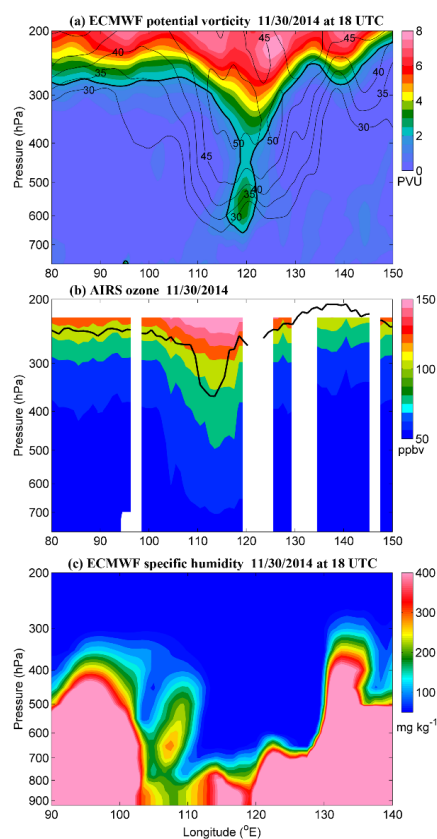
654



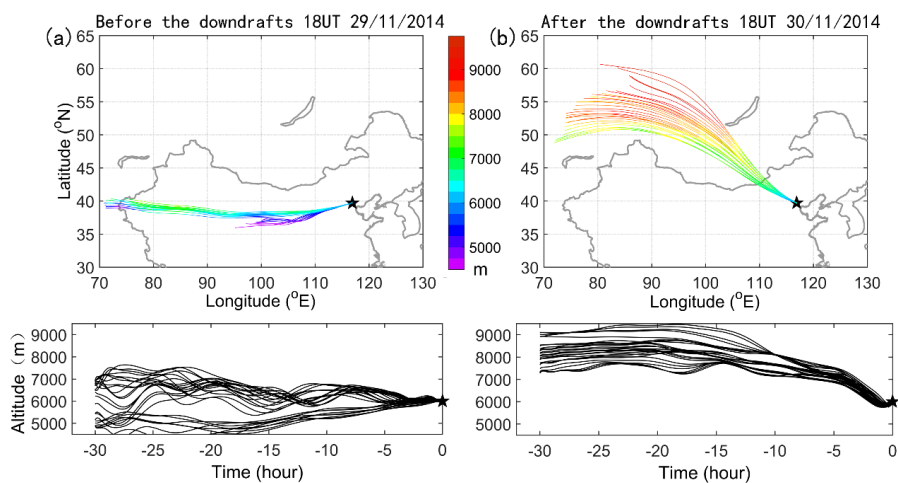
655

656 **Figure 8.** 500 hPa Ozone (left panels) and methane CH₄ (right panels) distribution
657 along with the tropopause height contour, derived from the AIRS satellite observations.
658 The top and bottom plots show the data of 30 Nov. 2014 and 1 Dec. 2014, respectively.
659 The black star indicates the location of Xianghe.

660

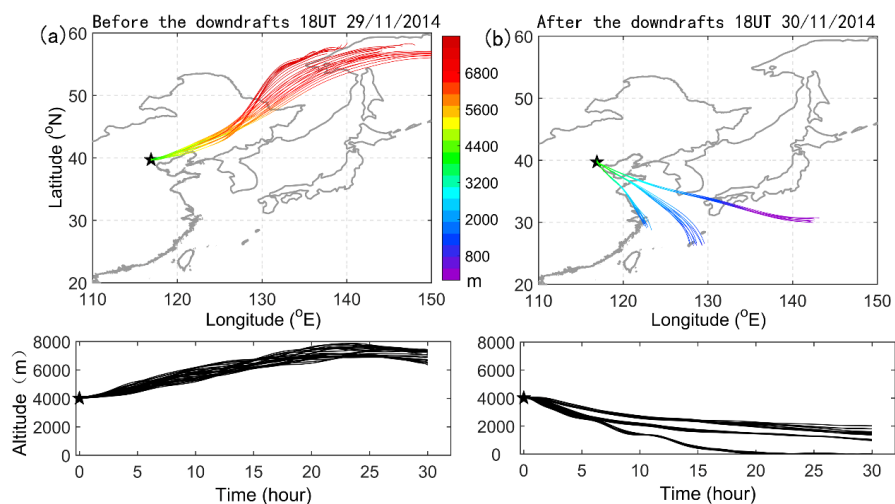


661
662 **Figure 9.** Longitude-pressure cross section of (a) ECMWF PV (colors, in pvu) along
663 with horizontal wind contour (thin black line, m/s) at 18 UTC on 30 Nov. 2014, (b)
664 AIRS ozone mixing ratio (colors, in ppbv) along with tropopause height (black line) on
665 30 Nov. 2014, and (c) ECMWF specific humidity (colors, in mg kg^{-1}) at 18 UTC on 30
666 Nov. 2014, at a constant latitude 40° N (nearest grid point in the latitude of Xianghe).
667 The bold line in (a) marks the isotropic line of PV at 2 pvu.



668

669 **Figure 10.** Illustration of 30 h three-dimensional backward trajectories ending at
670 Xianghe using National Oceanic Atmospheric Administration (NOAA) HYSPLIT
671 model: (a) before the main downdrafts at 18 UT on 29 November 2014, and (b) after
672 the main downdrafts at 18 UT on 30 November 2014. The HYSPLIT ensemble consists
673 of 27 trajectories. Upper plots show the horizontal projection of the trajectories, and the
674 lower plots show the corresponding time-height vertical displacement of the trajectories.
675

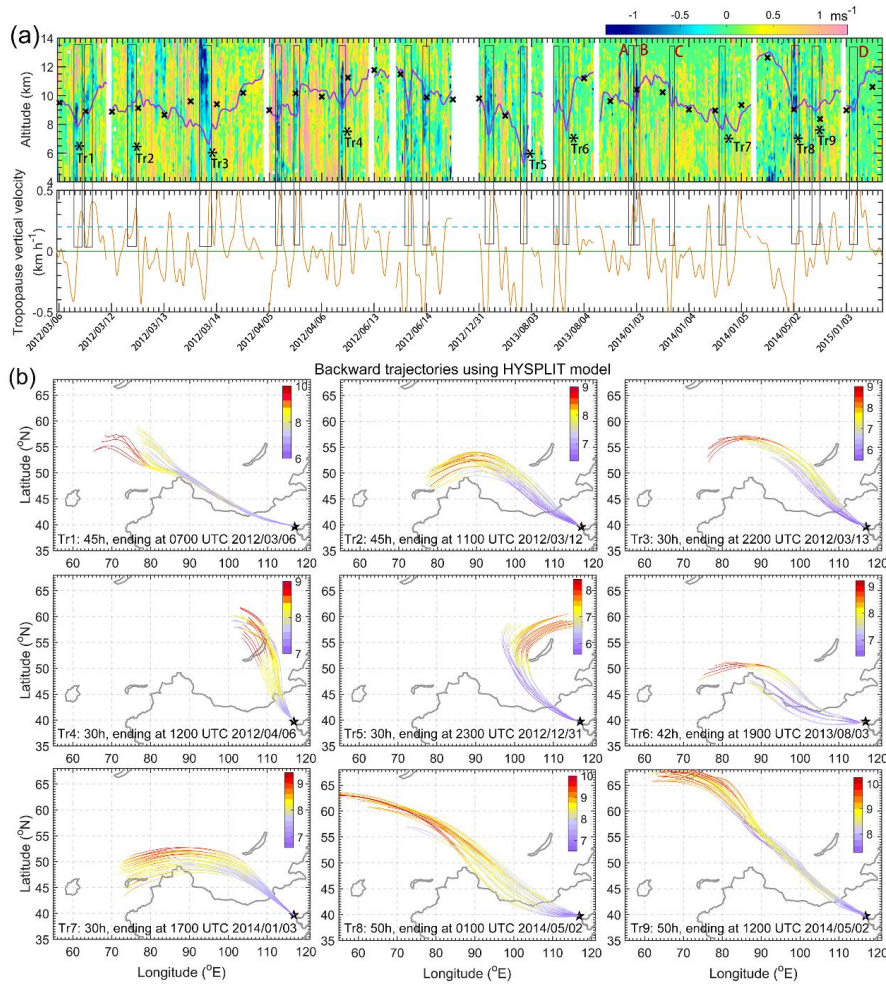


676

677 **Figure 11.** Same as Fig.10 but for three-dimensional forward trajectories starting at

678 Xianghe: (a) before the main downdrafts at 00 UT on 30 November 2014, and (b) after

679 the main downdrafts at 00 UT on 1 December 2014.

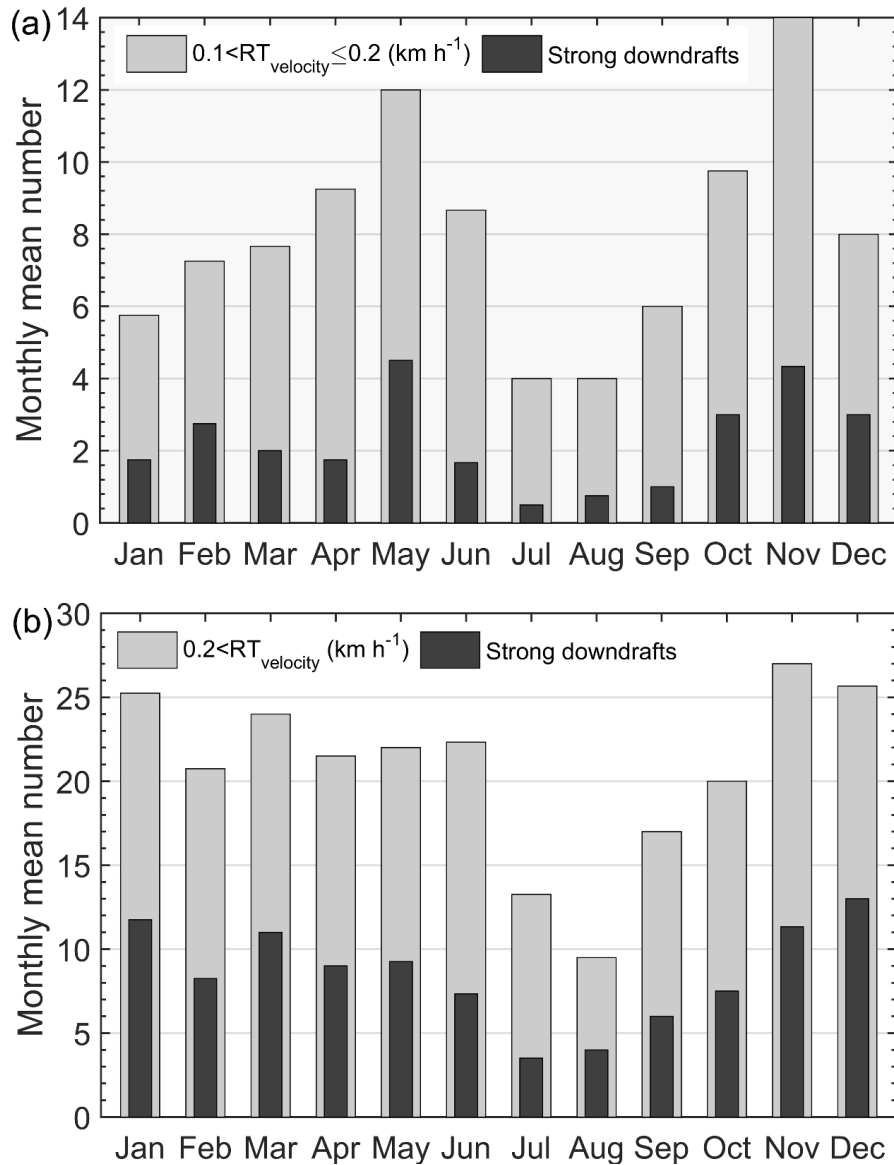


680

681 **Figure 12.** (a) Height-time section of several episodic observations of the radar-derived
 682 vertical wind (colors in m/s) along with RT height (purple bold line) and LRT height
 683 (bold crosses), between Mar. 2012 and Jan. 2015. The corresponding vertical velocity
 684 of the RT (orange line) is plotted in the lower panel of (a), dotted blue line indicates the
 685 value of 0.2 km/h. Dates for the observations are displayed as year/month/day. Black
 686 rectangular boxes represent the strong downdraughts (absolute value ≥ 0.5 m/s)
 687 observed just preceding rapid tropopause ascent (>0.1 km h⁻¹). Symbol ‘*’ labeled as



688 Tr1-Tr9 indicates the ending point of the corresponding trajectories in Fig.12b. (b)
689 Results of backward trajectories (colors in km) of the typical 9 selecting cases from
690 Fig.12a, providing the signature and source of possible stratospheric intrusions.
691



692

693 **Figure 13.** Four years (2012-2015) of radar-determined monthly mean number of rapid

694 tropopause ascent (gray bands) and the corresponding strong downdrafts just preceding

695 the rapid tropopause ascent (black bands). (a) Gray bands: with the ascent by at least

696 0.6 km and the excursion velocity is between 0.1-0.2 km h⁻¹; black bands: except for

697 the criteria of gray bands, strong downdrafts occurred preceding the rapid RT ascent



698 must exceed 0.5 m s^{-1} and pass through the RT layer. (b) Same as (a) but for the
699 occasions when the ascent velocity is larger than 0.2 km h^{-1} . According to the study
700 here, the black bands in the histogram well represent the occurrence of possible
701 stratospheric intrusions.